
White Rose Research Online

eprints@whiterose.ac.uk
https://eprints.whiterose.ac.uk
Universities of Leeds, Sheffield and York

Deposited via The University of Leeds.

White Rose Research Online URL for this paper:
https://eprints.whiterose.ac.uk/id/eprint/111051/

Version: Published Version

Article:
Hawthorne, JC and Rubin, AM (2010) Tidal modulation of slow slip in Cascadia. Journal of Geophysical Research, 115 (B9). ARTN B09406. ISSN: 0148-0227

https://doi.org/10.1029/2010JB007502

Copyright 2010 by the American Geophysical Union. Reproduced in accordance with the publisher's self-archiving policy.

Reuse
Items deposited in White Rose Research Online are protected by copyright, with all rights reserved unless indicated otherwise. They may be downloaded and/or printed for private study, or other acts as permitted by national copyright laws. The publisher or other rights holders may allow further reproduction and re-use of the full text version. This is indicated by the licence information on the White Rose Research Online record for the item.

Takedown
If you consider content in White Rose Research Online to be in breach of UK law, please notify us by emailing eprints@whiterose.ac.uk including the URL of the record and the reason for the withdrawal request.



Tidal modulation of slow slip in Cascadia

Jessica C. Hawthorne[1] and Allan M. Rubin[1]

Received 23 February 2010; revised 17 May 2010; accepted 11 June 2010; published 18 September 2010.

[1] Several studies have shown that the seismic tremor in episodic tremor and slip is tidally modulated, suggesting a sensitivity to the rather small tidal stresses. We address whether the slip rate in slow slip events is also tidally modulated by examining data from six borehole strainmeters in northwest Washington and southern Vancouver Island. We simultaneously fit data from multiple stations and from slow slip events occurring over a 3 year interval from January 2007 to June 2009, as we are unable to extract a meaningful signal from a single record. We find modulation of the strain rate with a 12.4 h period, that of the tide with the largest amplitude, that is significant at the 99% level. The amplitude of this modulation suggests that the slip rate during slow slip events oscillates, on average, 25% above and below its mean value during a tidal cycle. Tidal modulation estimates at three other periods are significant with more than 70% probability. The phase of maximum strain rate in the 12.4 h M2 period coincides with the phase of the maximum tremor rate taken from a catalog in an overlapping region. Comparison with a simple tidal loading model shows that the phase of maximum strain rate in the M2 period may occur at the maximum shear stress or up to 90° before it, depending on the location of slip in the subduction zone.

Citation: Hawthorne, J. C., and A. M. Rubin (2010), Tidal modulation of slow slip in Cascadia, *J. Geophys. Res.*, *115*, B09406, doi:10.1029/2010JB007502.

1. Introduction

[2] Slow slip events and accompanying tremor have now been observed at numerous subduction zones around the world. Events recur with periods from a few months to years and last from a few days to several years [e.g., *Schwartz and Rokosky*, 2007]. The extended event durations have allowed observers to track tremor over the course of weeks [e.g., *Kao et al.*, 2007; *Shelly et al.*, 2007; *Maeda and Obara*, 2009; *Wech et al.*, 2009]. Analysis of tremor during slow slip episodes has revealed a sensitivity to applied stresses much smaller than the ambient lithostatic pressure. Tidal stresses, with magnitudes of 0.1 to a few kPa, have been observed to modulate tremor amplitude and duration [*Shelly et al.*, 2007; *Nakata et al.*, 2008; *Rubinstein et al.*, 2008; *Lambert et al.*, 2009; *Thomas et al.*, 2009]. In Cascadia, studies have revealed a periodicity in tremor amplitude near the tidal frequencies [*Rubinstein et al.*, 2008] and a correlation of tremor occurrence with tidal shear stress [*Lambert et al.*, 2009]. Tremor on the San Andreas Fault occurs most frequently near the maximum favorable shear stress [*Thomas et al.*, 2009]. In Japan, swarms of tremor lasting a few hours recur with periods near 12 and 24 h [*Shelly et al.*, 2007; *Nakata et al.*, 2008; *Maeda and Obara*, 2009]. Comparison with a tidal loading model suggests that at least some of these tremor swarms occur between the maximum tidal Coulomb stressing rate and the maximum Coulomb stress [*Nakata et al.*, 2008]. Further confirmation that small stresses can influence tremor has come from triggering by dynamic stresses produced by earthquakes. Passing seismic waves causing stresses of several to tens of kPa sometimes trigger the occurrence of tremor outside of major slow slip events [e.g., *Rubinstein et al.*, 2007; *Gomberg et al.*, 2008; *Miyazawa and Brodsky*, 2008; *Rubinstein et al.*, 2009].

[3] While the processes involved in tremor and slow slip are not well known, the connection between them is well established. In all but a few cases, slow slip events coincide in time and space with the occurrence of tremor [e.g., *Rogers and Dragert*, 2003; *Obara et al.*, 2004]. The onset of strain signals due to slow slip in Cascadia is close in time to the onset of nearby tremor [*McCausland et al.*, 2008]. There is a tendency for the duration of recorded tremor to increase with the moment in slow slip [e.g., *Hiramatsu et al.*, 2008; *Aguiar et al.*, 2009]. So given the tidal modulation of tremor, it seems reasonable to expect that slow slip is also affected by the tides. However, the influence of small stresses on slow slip, as opposed to tremor, has thus far been documented only in an increased occurrence of slow earthquakes during typhoons in Taiwan [*Liu et al.*, 2009]. To date, a tidal influence on slow slip has not been documented. In addition, it is not clear what the amplitude or timing of such a tidal effect should be. If we imagine that tremor occurs in just a small part of the fault that is sensitive to very small stresses, tremor may be tidally modulated while slow slip is minimally affected. Alternatively, tremor may occur all over the

[1]Department of Geosciences, Princeton University, Princeton, New Jersey, USA.

Copyright 2010 by the American Geophysical Union.
0148-0227/10/2010JB007502

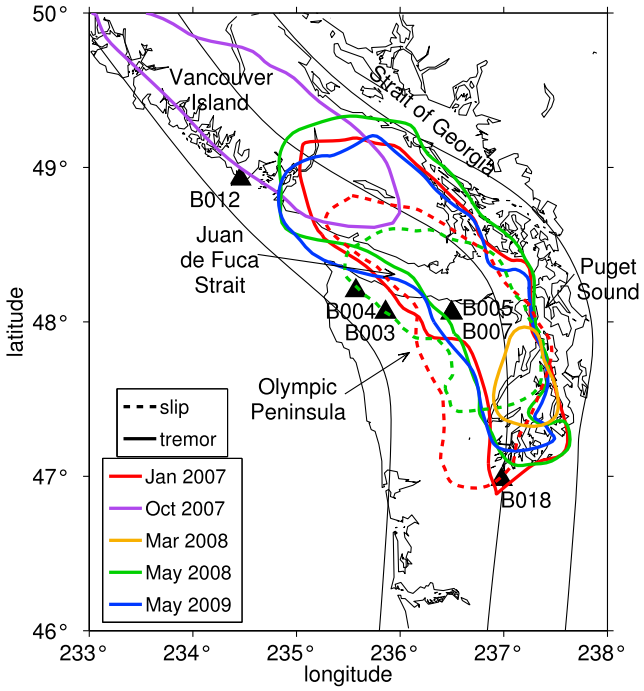

Figure 1. Map of borehole strainmeter sites. Triangles are station locations, and the thin black lines mark the location of the 20, 40, and 60 km depth contour of the Juan de Fuca slab [*McCrory et al.*, 2004]. The colored lines outline the approximate extent of slip (dashed lines) and tremor (solid lines) in each event. Slip extents are from *Wech et al.* [2009]. Tremor extents are from the online catalogs associated with *Wech and Creager* [2008] and *Kao et al.* [2009].

fault in response to slip, in which case the fractional changes in slip rate and tremor rate might be similar. In this paper, we attempt to constrain the presence, amplitude, and timing of changes in slip rate due to the tides. To do so, we examine the strain produced at the surface during slow slip events in northern Cascadia, as recorded by borehole strainmeters.

[4] The six strainmeters used are run by the Plate Boundary Observatory (PBO) and are located in northwest Washington and on Vancouver Island (Figure 1). Strainmeters are ideal for this work because they are sensitive to smaller magnitudes of slip and have a shorter effective time resolution than GPS. Two strain records from a slow slip event in May 2008 are shown in Figure 2. These strains and others of magnitude around 10^{-7} recorded at PBO stations in Cascadia have been interpreted as the result of several centimeters of slip on the plate interface near 40 kilometers depth [*McCausland et al.*, 2008; *Wang et al.*, 2008; Roeloffs et. al., Transient strain associated with nonvolcanic tremor in the northern Cascadia subduction zone from Plate Boundary Observatory borehole strainmeters, Earthscope National Meeting, Boise, Idaho, 2009]. In the component shown, the sign of the accumulating strain changes as the slow slip event migrates along the subduction zone and the location of slip relative to the borehole moves [e.g., *McCausland et al.*, 2008]. This migration and the resulting changes in strain rate at a single station occur over the course of one to three weeks. In this study we are interested in changes on shorter time scales, the diurnal and semidiurnal periods of the ocean loading and solid earth tides. We find that while noise in the data makes it impossible to extract the subdaily changes in slip rate from a single strain record, by using data from a number of stations and slow slip events we can reduce the error bars on an

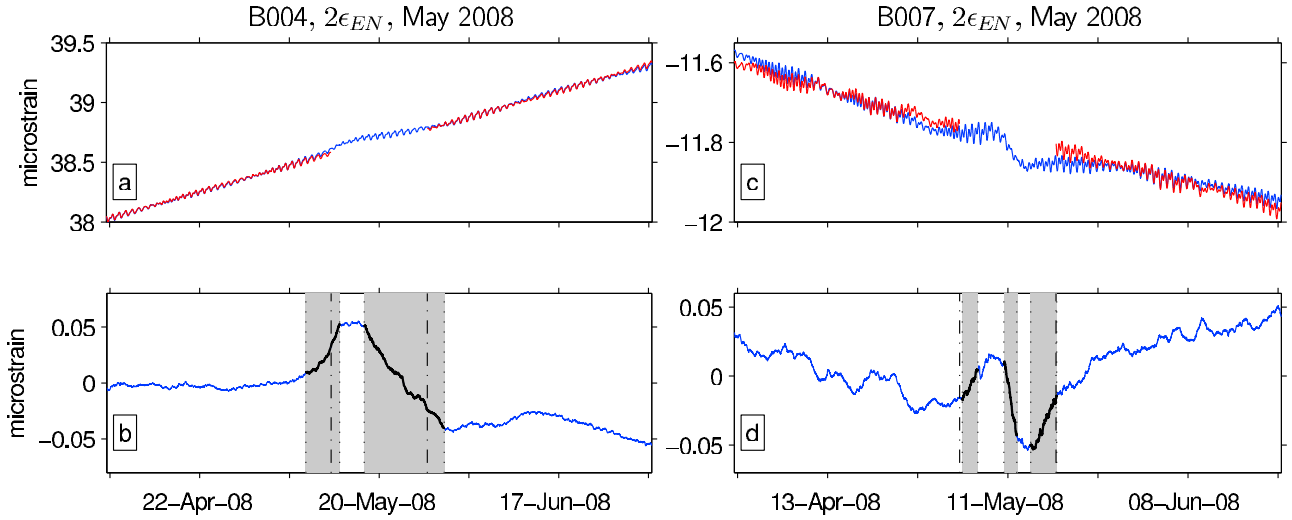

Figure 2. (a) Strain record of the engineering shear component at station B003 during the May 2008 slow slip event. Blue is the original data, and red is the fit for the corrections during the 35 days before and after the slow slip event. (b) The corrected data, after subtracting the fit with equation (1). Vertical dash-dotted lines bound the 15 day interval identified for the slow slip event, and the shaded regions define chosen segments with approximately constant strain rate, as discussed in section 3.2. (c, d) As in Figures 2a and 2b, but for station B007. In some stations and components, such as that in Figure 2b, the chosen segments extend slightly outside the 15 day window. This has a minor effect on the tidal correction fit and is accepted so that all the data may be processed uniformly.

average strain rate to a small enough level to observe tidal modulation. We begin in the next section by introducing the strain data and some necessary processing steps. In section 3 we describe how we look for a tidal modulation signal in the strain data, and in section 4 we present our results and error estimates. Finally, we compare the strain estimates with a forward model of tidal loading and with observations of tremor in section 5.

2. Data Processing

[5] Each strainmeter consists of four horizontal extensometers located at depths of a few hundred feet. In the processed data provided by PBO, these data have been converted to three horizontal strain components, downsampled to a 5 min interval, and filtered for outliers and known instrumental errors. Because the areal strain appears to have a larger uncertainty and greater coupling to atmospheric pressure, in this study we use only the two horizontal shear strain components $2\epsilon_{EN}$ (engineering shear, including N to the E and E to the N simple shear) and $\epsilon_E - \epsilon_N$ (the difference in extension along these two axes). The strainmeters were installed between 2004 and 2006, and we use data during three major slow slip events in January 2007, May 2008, and May 2009, as well as during smaller episodes with tremor and observable strain in October 2007 [e.g., *Kao et al.*, 2009] and March 2008 [e.g., *Wech and Creager*, 2008].

[6] In order to detect variations in strain of the magnitude we are interested in, we first need to correct for a number of undesired signals in the data. These include borehole curing, deformation due to atmospheric pressure, and the direct local deformation caused by the ocean loading and body tides. Some of these signals are quite large. In the case shown in Figure 2c, the amplitude of strain produced by direct tidal loading is comparable to that produced by slow slip, but it occurs over the course of 1 day rather than 1 week, so that the strain rate produced by the direct tidal loading is 1 order of magnitude larger than that produced by slow slip. It is important to eliminate as much of these unwanted signals as possible so that we can look for tidal modulation of slow slip. To do so, we compute an empirical correction using strain data recorded close to but not during each slow slip event. For each borehole station and component, we identify a 15 day interval that includes the large majority of the slow slip strain. We perform the following least squares fit to the 35 days before and after this interval:

$$\epsilon_i = c_1 + c_2 t_i + c_3 p_i + c_4 H(t_i - t_{ss}) + \sum_{k=1}^{17} [a_k \cos(2\pi t_i / T_k) + b_k \sin(2\pi t_i / T_k)]. \quad (1)$$

Here ϵ_i is the recorded strain at time t_i, p_i is the barometric pressure recorded at the station location, t_{ss} is any time during the slow slip interval, and the T_k's are the 17 tidal frequencies we wish to remove. $H(t)$ is the Heaviside function. This fourth term is included to avoid biasing the linear trend, as some net strain is accumulated during the slow slip event, but it is not a correction to be removed. After obtaining the best fitting a_k, b_k, and c_1–c_4, we evaluate the correction terms (not including the c_4 term) in the entire 85 day interval including the 15 day slow slip interval, and subtract the result from the original data to obtain the processed data used in the rest of this paper. The length of the 15 day slow slip and 35 day adjacent intervals were found by trial and error to visually best fit the data. The 17 tides removed are, with periods in hours: Q1, 26.8684; O1, 25.8193; NO1, 24.8332; P1, 24.0659; S1, 24.0000; K1, 23.9345; J1, 23.0985; OO1, 22.3061; e2, 13.1272; MU2, 12.8718; N2, 12.6583; M2, 12.4206; L2, 12.1916; S2, 12.0000; K2, 11.9672; et2, 11.7545; M3, 8.2804. The clusters of periods at around one day (P1, S1, K1) and one-half day (S2, K2) are included despite having very similar frequencies because using only one frequency for each group clearly worsens the fit to the data.

3. Tidal Modulation Fits

3.1. Data and Noise Level

[7] If the processed data were noise-free, the strain record would have zero slope outside the slow slip event, and would contain the slow slip signal, possibly tidally modulated, during the event. Given a modest amount of noise, a clear signal of tidal modulation could still be recognized if the power spectrum during all or part of the slow slip event was peaked at tidal frequencies, and if in addition these peaks were larger than those at the corresponding tidal periods at times outside the slow slip window. Taking the Fourier transform of the data in Figures 2b and 2d, or even a visual inspection, reveals that after processing there is still considerable energy in the tidal band during the slow slip event. However, one cannot associate this readily apparent signal with tidal modulation of slow slip, for two reasons. First, the power at tidal frequencies is not obviously larger during the slow slip event than during the 35 day adjacent intervals, or during randomly chosen portions of the data processed in the same way as for the slow slip sections. Second, the changes in strain rate during the slow slip events seem too large to be consistent with reasonable models of tidal modulation. Note that even if slow slip is strongly modulated, the sense of slip is not expected to reverse during a portion of the tidal cycle; the slip rate may approach zero but seems exceedingly unlikely to become negative. The accumulating strain due to slip is likewise expected to retain the same sign throughout the tidal cycle. This is not the case in parts of the corrected data shown in Figures 2b and 2d, nor in a number of other records, implying that the readily apparent signal often has amplitude larger than the largest physically plausible signal we are interested in. Such large amplitudes are not restricted to the slow slip intervals. Strain rates in portions of the data outside slow slip events are often large enough to make a typical slow slip signal change sign. We must therefore identify much if not most of the apparent strain signal as noise.

[8] From these considerations we conclude that we cannot say anything about the presence or absence of tidal modulation of slow slip from a single station record. However, we can improve the signal-to-noise ratio by stacking data from multiple stations, components, and slow slip events. To this end, we design a fit to the data (described in section 3.3) that assumes that the tidal signal maintains the same phase in all

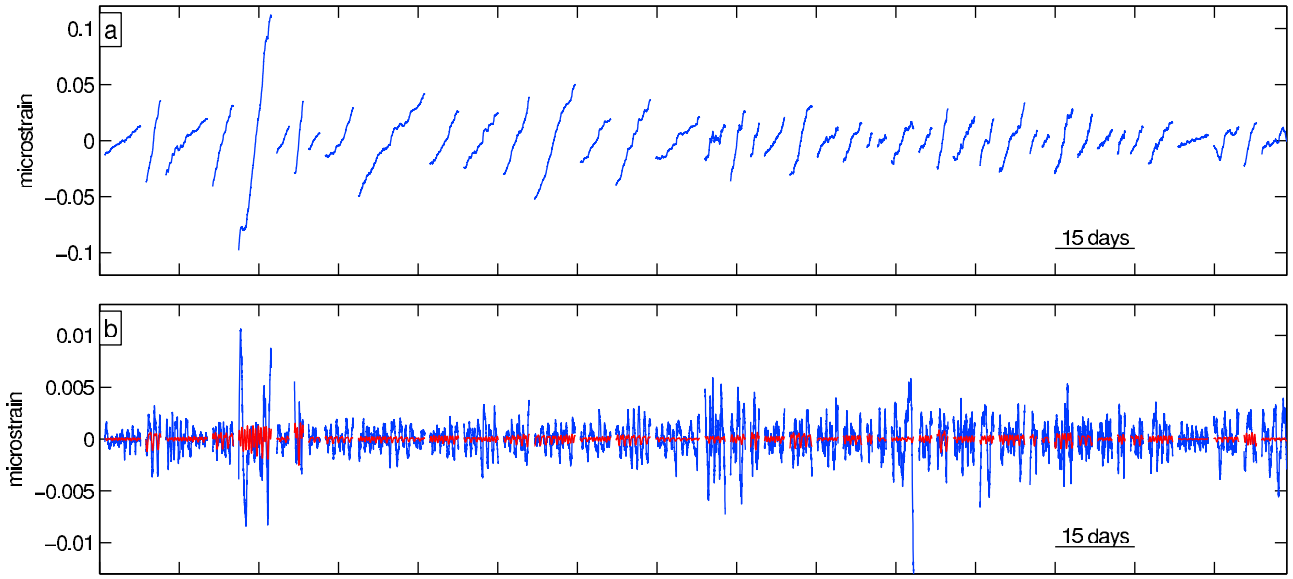

Figure 3. (a) All of the approximately linear strain segments chosen pasted end to end, after removing the mean and flipping segments so that strain is increasing in all cases. (b) Blue: the same segments, but after highpass filtering the data and removing a linear trend from each segment. Red: the fit to the data with equation (5). Note that most of the variability visible outside of the linear trend is due to noise; that is, it cannot be fit by these four tidal periods with a single amplitude and phase for each.

records. Such an assumption reduces the fit's sensitivity to noise since none of the sources of noise are expected to be correlated over most of the stations and events. In contrast, any tidal modulation of slow slip should result in a high slip rate during a well-defined part of the tidal loading cycle. If the phase of the loading on the plate interface does not change appreciably from event to event or from station to station, signals at the tidal frequencies should have the same phase in all the strain records. The ocean loading and body tides do not change significantly in three years, so the phase of any tidal modulation should remain the same in all similarly located slow slip events. In the computations presented in section 5.1, the phase of tidal loading varies along the subduction zone by one quarter cycle for the semidiurnal tides, which include the largest-amplitude tide, and one-half cycle for the diurnal tides. This range of phases is small enough that fitting data from multiple stations with a single phase is adequate for our purposes and for the noise level in the data, as discussed in section 4.3.1.

[9] One adjustment of the expected phase of the maximum strain rate is required. It is clear from Figures 2b and 2d that slow slip produces both positive and negative strain rates depending on the location of slip with respect to the strainmeter. This means that a tidally enhanced slip rate would result in a more positive strain rate in portions of the data where strain is increasing and a more negative strain rate in portions of the data where strain is decreasing. We account for this by flipping the sign of the strain in portions of the data where slow slip causes decreasing strain, so that we always model strain as increasing due to slip.

3.2. Isolating Data Segments

[10] In this paper, we do not attempt to model the evolution of strain throughout the entire slow slip event, as this would require knowledge of the changing location of slip. We isolate and consider only relatively simple portions of the processed data. In each strain record, we identify segments where strain changes approximately linearly with time. Several of these segments are marked by the shaded regions in Figures 2b and 2d. Most of the chosen segments are three to five days long, long enough to capture a diurnal signal but short enough that the migration of the slipping patch has a minor influence. We assume that within each segment changes in strain rate on a diurnal or semidiurnal time scale are dominated by and approximately proportional to changes in slip rate. 44 segments are chosen from all stations, components, and events; these are plotted end to end in Figure 3a, and they are listed in Table 1. Segments are only chosen in portions of the data that clearly exhibit slow slip, and when it is possible to identify sections that are approximately linear. Given the variable noise level at each station, and the different locations and magnitudes of slip in each event, appropriate segments cannot be confidently identified in all slow slip events at each station.

[11] Segments are picked to be dominated by a linear trend, but there is nevertheless some change in the strain rate due to a combination of long-term changes in slip rate and migration of the slip location during any several day interval. To exclude as much of the migration signal as possible from our analysis, we highpass filter the data after choosing but before extracting the segments. The filter applied is zero below 0.4 cycles per day and increases to one at 0.6 cycles per day along one half of a cosine curve. This removes signals with periods longer than two days from the 85 day strain record.

3.3. Strain Rate Model

[12] Since we have attempted to remove all other signals, the strain in each segment is assumed to be the result of a constant slip rate, potentially modulated by the tidal

Table 1. List of the 44 Segments Used[a]

Station	Component	Segment Start	Segment Finish	Center of Correction Fit Interval
B003	$2\epsilon_{EN}$	30 Apr, 22:20	7 May, 16:18	9 May 2008
		11 May, 22:25	14 May, 17:19	9 May 2008
		14 May, 20:50	22 May, 15:27	9 May 2008
		12 May, 03:26	16 May, 01:20	10 May 2009
	$\epsilon_E - \epsilon_N$	6 May, 11:29	12 May, 15:22	10 May 2009
B004	$2\epsilon_{EN}$	26 Jan, 12:10	28 Jan, 20:50	31 Jan 2007
		30 Jan 12:30	1 Feb, 04:10	31 Jan 2007
		2 Oct, 11:29	4 Oct, 14:29	2 Oct 2007
		8 May, 13:21	13 May, 20:06	20 May 2008
		17 May, 15:39	30 May, 02:57	20 May 2008
		7 May, 10:07	12 May, 19:37	15 May 2009
		16 May, 20:45	23 May, 08:10	15 May 2009
	$\epsilon_E - \epsilon_N$	26 Jan, 20:40	31 Jan, 16:50	31 Jan 2007
		11 May, 01:12	18 May, 16:18	20 May 2008
		27 May, 22:08	2 Jun, 15:27	20 May 2008
		11 May, 09:01	17 May, 20:50	22 May 2009
		26 May, 08:49	3 Jun, 15:08	22 May 2009
B005	$2\epsilon_{EN}$	18 Jan, 15:17	22 Jan, 10:50	27 Jan 2007
		25 Jan, 02:13	27 Jan, 21:07	27 Jan 2007
		30 Jan, 08:59	31 Jan, 23:43	27 Jan 2007
		3 May, 21:44	7 May, 16:23	10 May 2008
		9 May, 00:46	13 May, 05:08	10 May 2008
		14 May, 07:02	18 May, 04:56	10 May 2008
		6 May, 15:09	7 May, 14:53	10 May 2009
		9 May, 14:20	13 May, 01:23	10 May 2009
		14 May, 16:22	16 May, 07:21	10 May, 2009
B007	$2\epsilon_{EN}$	24 Jan, 08:34	28 Jan, 12:57	27 Jan 2007
		3 May, 21:44	6 May, 08:00	11 May 2008
		10 May, 09:08	12 May, 09:42	11 May 2008
		14 May, 13:31	18 May, 14:39	11 May 2008
		5 May, 03:40	7 May, 18:00	10 May 2009
		9 May, 04:00	14 May, 00:09	10 May 2009
		14 May, 05:49	15 May, 12:59	10 May 2009
B012	$2\epsilon_{EN}$	3 Oct, 09:08	4 Oct, 17:31	7 Oct 2007
		6 Oct, 14:51	9 Oct, 23:47	7 Oct 2007
	$\epsilon_E - \epsilon_N$	4 Oct, 04:34	6 Oct, 21:19	7 Oct 2007
		29 May, 04:43	31 May, 23:07	3 Jun 2008
		1 Jun, 00:57	2 Jun, 12:00	3 Jun 2008
B018	$2\epsilon_{EN}$	2 Mar, 13:40	4 Mar, 22:20	6 Mar, 2008
		17 May, 06:40	21 May, 20:45	22 May 2008
		16 May, 11:12	22 May, 04:31	15 May, 2009
	$\epsilon_E - \epsilon_N$	2 Mar, 16:30	7 Mar, 09:50	6 Mar 2008
		6 May, 15:00	8 May, 23:21	10 May 2009
		9 May, 09:54	14 May, 02:35	10 May 2009

[a]The second and third columns give the segment endpoints. The center of both the 15 day slow slip window and the 85 day window used for removing direct tidal and long-term signals is midnight on the day listed in the fifth column.

stress. This leads to a model of the strain rate as a constant plus a set of sinusoids at the tidal periods:

$$\frac{d\epsilon}{dt} = \text{constant} + \sum_k C_k \cos\left(t\frac{2\pi}{T_k} - D_k\right), \quad (2)$$

where ϵ is strain, t is time, and C_k and D_k are the amplitudes and phase lags of the signal at periods T_k. The periods of four of the largest tides (M2, S2, O1, and K1) are used (see Table 2 for the periods). As we have argued above that the tidal loading is approximately in phase for all our strain records, the phase of any tidal modulation of the strain rate should be approximately constant from segment to segment. In the simplest possible case, one could imagine that the amplitude C_k is also constant from segment to segment, leading to the fit:

$$\epsilon_i = k_{m_i}(t_i - \bar{t}_{m_i}) + \sum_{k=1}^{4}[A_k \cos(2\pi t_i/T_k) + B_k \sin(2\pi t_i/T_k)]. \quad (3)$$

The parameters to be fit in this case are the tidal modulation coefficients A_k and B_k. ϵ_i is the corrected strain at time t_i, with the mean removed from each segment, and $\bar{t}_m$ is the

Table 2. Amplitudes and Phase Lags of Mean Tidal Stresses[a]

	Shear Stress		Normal Stress	
Period (h)	Amplitude (kPa)	Phase Lag (deg)	Amplitude (kPa)	Phase Lag (deg)
12.4206 (M2)	0.81	−80	0.75	62
12.0000 (S2)	0.25	81	0.28	−140
12.6583 (N2)	0.16	32	0.14	171
25.8193 (O1)	0.15	−148	0.96	−34
23.9345 (K1)	0.24	−18	1.58	94

[a]Stresses are averaged between 30 and 50 km depth and 46 and 50 degrees north. Amplitudes are one-half peak to trough. Phase lags are the delay of the peak stress relative to 1 January 2000. Normal stress has tension positive. The N2 tidal period is not used to fit the strain data because signal at this period appears to trade off with signal at the M2 period.

mean time in segment m. The fit is performed on the highpass filtered data, so the initial linear trend has been removed, but k_m is still included as a free parameter to allow for any residual linear trend in each segment. It is generally quite small compared with the linear trend in the unfiltered data.

[13] The fit above assumes that the amplitudes of the strain rate changes produced by the tidal forcing are the same from station to station. We have used equation (3) to fit the data as a test because relating the uncertainties in the original data to uncertainties in the modulation estimates is relatively simple with this fit. However, the strain rate at a given station is not merely a function of the slip rate; it also depends on the component orientation and station location. If we assume that the strain rate at a particular station is proportional to fault slip rate, then one might expect that the amplitude of the strain rate modulation is proportional to the observed mean strain rate, as in

$$\frac{d\epsilon}{dt} = \text{constant} \times \left(1 + \sum_k \gamma_k \cos\left(t\frac{2\pi}{T_k} - \delta_k\right)\right). \quad (4)$$

Now requiring that the scaled amplitudes γ_k be constant from segment to segment is equivalent to assuming that the fractional increase in slip rate from tidal modulation is the same at all times and locations. With this assumption, and the assumption of constant phase in all segments, the appropriate fit to the strain records is

$$\epsilon_i = k_{m_i}(t_i - \bar{t}_{m_i}) + \sum_{k=1}^{4} l_{m_i}\frac{T_k}{2\pi}[\alpha_k \cos(2\pi t_i/T_k) + \beta_k \sin(2\pi t_i/T_k)]. \quad (5)$$

Here l_m is the mean strain rate in segment m, and is found from a linear least squares fit to the unfiltered data. Then equation (5) is fit to the filtered data. In this fit, the scaled tidal modulation amplitudes $\gamma_k = \sqrt{\alpha_k^2 + \beta_k^2}$ are reported as fractions of the mean strain rates $\bar{l}_m$. For example, if $\gamma = 1$ the fault would stop slipping at one point in the tidal cycle and slip at twice the mean rate at another time. Equation (5) is our preferred fit to the data.

[14] One additional complication to the fit is introduced by the fact that the amplitude of the noise varies strongly from segment to segment. Doing a simple least squares fit to the data overweights certain stations and components. As we have established that the dominant variability in a slow slip record is from noise, not tidal modulation, we use the variance in each segment as an estimate of the noise. This variance is computed after removing a linear trend from each segment. The detrended data are shown by the blue lines in Figure 3b. When a fit is done, the error at each point is downweighted by the variance in the segment that point belongs to. This is equivalent to doing an unweighted least squares fit after dividing equation (3) or (5) by the standard deviation in segment m_i. Also plotted in Figure 3b (the red curve) is the best fitting tidal component computed with equation (5) and with the error weighting just described. It is clear that most of the variability in each segment is not accounted for by the fit, which is consistent with our assumption that the variance in any segment gives an estimate of the noise. This is true even if we perform the fit without weighting the error in each segment differently or if we use equation (3) to fit the data.

[15] In all of the results shown in this paper, sinusoids at all four frequencies are fit simultaneously. We have experimented with fitting each of these four frequencies alone and obtain almost identical results. However, signal at the 12.7 h N2 tidal period is not included because it appears to trade off with the 12.4 h M2 period signal. These four tidal frequencies used are chosen because they are known to be the periods of the strongest tides. In Appendix A we consider a much wider range of potential frequencies to address whether these tidal frequencies are in fact the strongest periodic signals in the data.

3.4. Residual Noise Levels

[16] As mentioned in the last section, it is immediately evident from Figure 3b that most of the variability in the data is not accounted for by the tidal fit; there is no set of four sinusoids with constant scaled amplitude and phase in all segments that can accommodate most of the signal. In fact, the tidal component of the fit reduces the weighted variance of the data by only about 5%. If we bandpass filter the data between 1.7 and 2.3 cycles per day, around the frequency of the largest-amplitude tide, the tidal fit accounts for 15% of the weighted variance. In section 4.1, we will show that even variance reductions this small allow us to constrain the amount of correlated tidal signal.

[17] Here, we show that the residual signal has magnitude appropriate for the noise level in these data. To do so, we compare the standard deviations in the 44 slow slip segments with those in segments at times outside of slow slip. The times of a set of "random" segments are obtained by shifting the times of all the slow slip segments forward or backward by some amount (the same for each segment). The data at these times are then processed in the same way as the data during slow slip to obtain a new set of segments. We apply the corrections as discussed in section 2, highpass filter the corrected data, and remove a linear trend. 300 overlapping sets of non-slow-slip segments are obtained, with time shifts at 0.66 day intervals from −150 to −50 and 50 to 150 days. Since these non-slow-slip segments were not picked by hand, in some cases abrupt signals or problems with the instrument cause poor correction fits and very high residual noise. We discard close to 10% of the time-shifted segments because they have standard deviations larger than 0.005 microstrain or dropouts in the data that precluded doing the empirical corrections at all.

[18] In Figure 4, we plot a histogram of the standard deviations in the remaining time-shifted segments, along with a histogram of the standard deviations in the 44 slow slip segments. The standard deviations in the slow slip segments are clearly larger, but only by a fraction of the mean; the variance is dominated by background noise. The median standard deviation in the slow slip segments is about 13×10^{-4} microstrain, compared with 8×10^{-4} microstrain in the non-slow-slip segments. This approximately 60% increase could be because of signal from slow slip at the tidal periods, from slow slip signal at a wide range of periods, or the slow slip segments could simply be in portions of the data with slightly larger noise, independent of any signal due to slow slip. This last seems unlikely, as fewer than 10 of the 300 sets of shifted segments have a

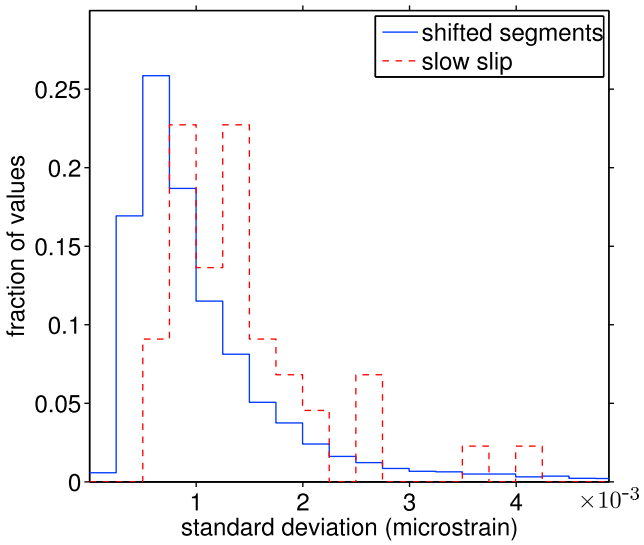

Figure 4. Histogram of the standard deviations in individual segments. The red dashed line is for the 44 chosen slow slip segments, and the blue solid line is for the segments not during slow slip events. Data are highpass filtered and a linear trend is removed from each segment before computing the standard deviation.

median standard deviation larger than that of the slow slip segments. To assess the possibility of the increased variance being due to slow slip, we can calculate the variance of sinusoids with plausible amplitudes given the mean strain rates in slow slip. Assuming an average slope in the slow slip segments of 0.01 microstrain per day, the amplitude of a sinusoid with period of 0.5 days corresponding to the maximum possible tidal modulation without the fault slipping backward would be $[0.01 \text{ microstrain d}^{-1}] \times [0.5 \text{ days}/(2\pi)] \approx 10^{-3}$ microstrain, leading to a standard deviation of $10^{-3}/\sqrt{2} \approx 7 \times 10^{-4}$ microstrain. So it is possible to account for a 60% increase in standard deviation by either tidal modulation of slow slip or by complexity in slow slip with variations in slip rate that are a modest fraction of the mean. However, most of this tidal modulation could not be coherent across all stations and events at the fitted frequencies, or the variance reduction would be significantly larger. In Appendix A we show that there is power in the slow slip segments at a range of periods, though the portion of that signal that is coherent across all events and stations is rather small, usually changing the strain rate by less than 10%. It thus seems reasonable to attribute most of the increase in variance during the slow slip segments to the intrinsic complexity of slow slip, resulting in variations in strain rate that are coherent only across a subset of the stations during a single event.

4. Tidal Modulation Estimates and Errors

[19] A fit to the data as in equation (3) or (5) results in an amplitude and phase lag of the tidal modulation at each frequency. In this section, we show the results of the fits and assess how accurately we can constrain the tidal modulation parameters. The best fitting tidal parameters are marked by x's in Figure 5. In these plots, the distance from the origin is the amplitude of the tidal modulation C_k (equation (3)) or γ_k (equation (5)), and the angle clockwise from the positive vertical axis is the phase lag of the peak strain rate D_k or δ_k, relative to the calculated phase lag of the maximum mean shear stress on the plate interface. This mean shear stress is calculated from the ocean loading and solid earth tides and will be discussed further in section 5.1. Note that in addition to a simple phase shift, the sign on the vertical axes in Figure 5 is reversed so that phase lag is positive clockwise. As can be seen in Figure 5b, the signal at the M2 tidal period has 99% confidence intervals that do not include the origin. Before discussing these results further we outline our procedure for obtaining error estimates.

4.1. Error Estimates

[20] Our first approach to calculating an error estimate is a bootstrap resampling of the slow slip segments. This involves repeatedly choosing and fitting some subset of the slow slip data. In each step, we randomly pick 44 of the 44 slow slip segments with replacement. On average, two thirds of the original segments are picked in each step, some of which are picked multiple times. We perform the original fit on this new set of data (including the duplicated segments) to obtain a single bootstrap parameter estimate. Repeating this 3000 times provides 3000 parameter estimates that approximate the probability distribution of the tidal modulation parameters given these data [e.g., *Efron and Tibshirani*, 1993]. In Figures 5a–5h we plot contours of a histogram of these estimates. The contour values indicate the number of parameter estimates in a box that is one thirtieth of the total box on each side. The black ellipses shown surround 90 and 99% of the 3000 modulation estimates. In Figures 5a–5d we use equation (5) to do the tidal fit, while in Figure 5e–5h we use equation (3). The axes in Figures 5e–5h are chosen such that the results would be identical to those in Figures 5a–5d if the mean strain rate in every segment were 0.01 microstrain per day.

[21] In our next approach to estimating the uncertainty of the modulation parameters, illustrated by the red ellipses in Figures 5i–5l, we estimate the coherent tidal signal in portions of the data not during slow slip. Just as was done to estimate the background noise level in section 3.4, a set of non-slow-slip segments is obtained by shifting the times of all the slow slip segments by some fixed amount, and then the data at these new times are processed and the tidal modulation amplitudes and phase lags are computed as with the slow slip segments. Segments with implausible standard deviations of more than 0.005 microstrain probably include errors in applying the corrections and are not used. Equation (5) is used to fit the data, and the amplitude of modulation in each of the time-shifted segments is assumed to be proportional to the mean strain rate in the corresponding slow slip segment. Since we have attempted to remove the direct tidal signal via equation (1), the non-slow-slip segments are not expected to contain a coherent signal at the tidal periods. Any nonzero tidal modulation estimate obtained comes from fitting unremoved noise. To the extent that the noise is similar during and outside the slow slip intervals, the estimated tidal modulation parameters for the non-slow-slip segments should approximate the error distribution for the slow slip modulation estimates. 90% confidence intervals for this method are shown in Figure 5, and are created by taking 300 equally spaced time

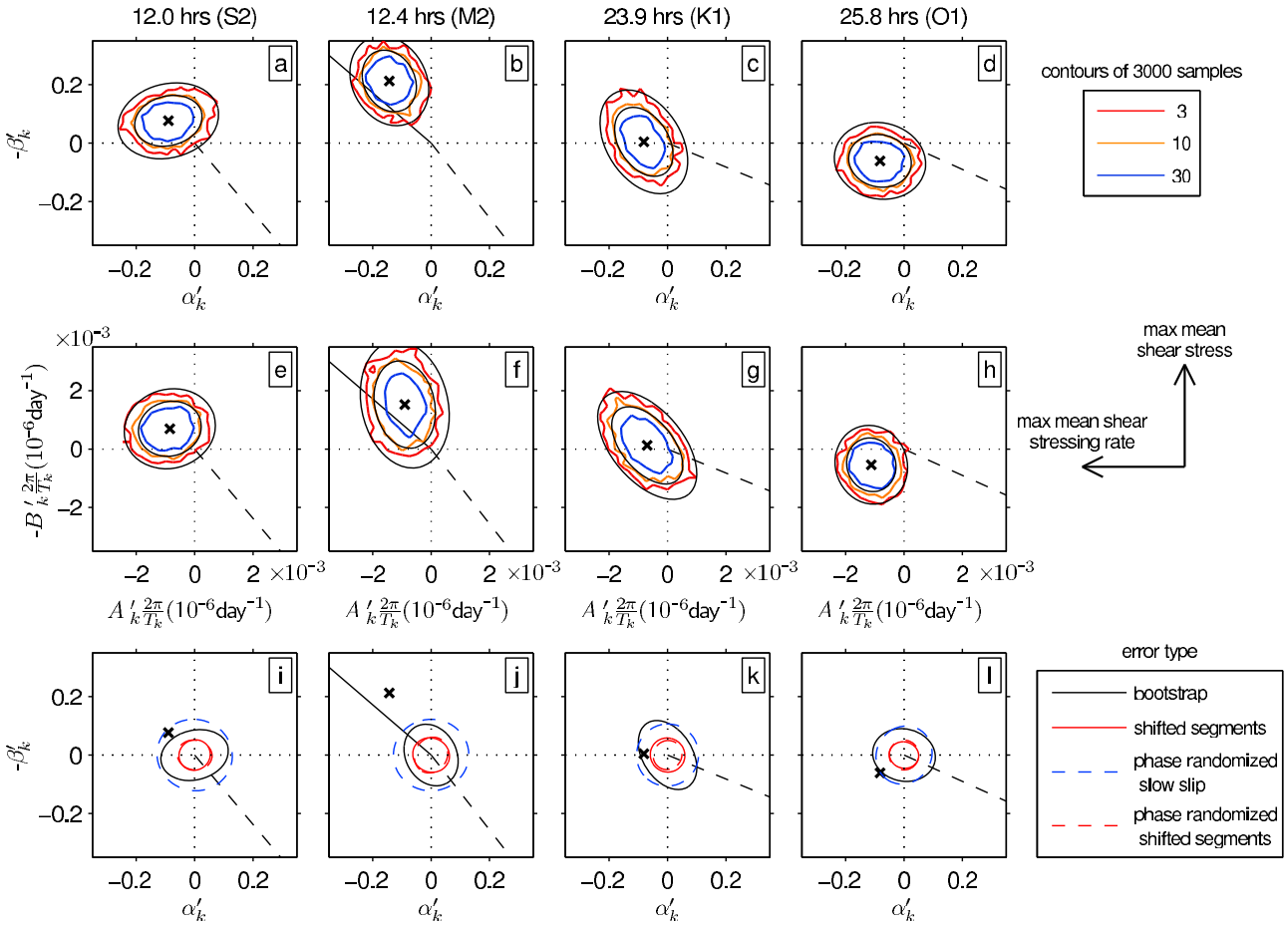

Figure 5. (a–d) Contours of the probability distribution of tidal modulation coefficients obtained with 3000 bootstrap resamplings fit with equation (5). Crosses mark the best fitting coefficients. The ellipses contain 90% or 99% of the bootstrap values in each panel. All coefficients are modified so that the angle clockwise from the positive y axis is the delay of the strain rate peak relative to the maximum shear stress from Table 2. Dashed radial lines indicate the phase of the maximum mean tensile normal stress. The solid radial lines in Figures 5b, 5f, and 5j indicate the phase of the best fitting sinusoid to the tremor histogram in Figure 7. (e–h) As in Figures 5a–5d, but for parameters fit with equation (3). (i–l) The 90% confidence ellipses for bootstrap, phase randomized slow slip, and shifted segments error estimates (see text). Dashed ellipses are for error estimates where each segment has been given a random phase shift. The bootstrap ellipses are shifted by the best fitting estimate of the tidal coefficients to be centered at the origin in Figures 5i–5l.

shifts between 150 and 50 days backward and between 50 and 150 days forward. As expected, these distributions are centered at the origin; in Figures 5i–5l the bootstrap distributions (shown by the black ellipses) are shifted to the origin for comparison.

[22] The coherent signal at tidal periods found in non-slow-slip segments may come from fitting noise that varies randomly from segment to segment or from fitting noise that for whatever reason is correlated across multiple stations and events. Correlated noise could be a large contributor to the uncertainty in the tidal modulation estimates if, for example, much of the residual signal is due to regional-scale weather systems or ocean loading changes. To address its importance, we make a new estimate of the uncertainty in the tidal modulation parameters from the non-slow-slip segments, but this time we attempt to eliminate any correlations between segments. The new set of distributions is computed in the same way as described in the previous paragraph, except that before the tidal fit the times (but not the data) in each segment are shifted by a random amount between zero and about 1.8×10^4 days, resulting in a random phase at all four periods. The new distributions, illustrated by the dashed red ellipses in Figures 5i–5l, are almost identical to the distributions from the non-slow-slip segments with no phase shift (solid red ellipses), which include all sources of noise. The lack of a decrease in the estimated coherent signal when the segments are assigned random phases suggests that the dominant source of noise is uncorrelated from segment to segment.

[23] We also follow a similar procedure to estimate the uncertainty due to uncorrelated noise using just the slow slip segments. In each step, we process the slow slip data as usual and fit sinusoids to the segments according to equation (5). However, before the fit the times in each segment are given

a random phase shift, eliminating the possibility of fitting a correlated signal. Confidence intervals from distributions obtained with 3000 phase randomizations and fits are shown by the dashed blue ellipses in Figures 5i–5l. The uncertainties tend to be slightly larger than those obtained by bootstrapping. This is surprising since the bootstrap errors should include at least some portion of the correlated as well as uncorrelated noise, but we note that the difference is not large, and the two error estimates are not as comparable as the two for the non-slow-slip segments. In both cases the signal at the M2 period is significant with more than 99% probability.

4.2. Results

[24] As can be seen in Figure 5b, the signal at the M2 tidal period has 99% confidence intervals from bootstrapping that do not include the origin. The best fitting amplitude of modulation at this period is 26% of the mean strain rate. If the null hypothesis that there is no tidal modulation were correct, there would be a less than 1% chance of obtaining an amplitude this large. Estimates of coherent signals at three other tidal periods are significant at the 70 to 90% level, with best fitting amplitudes of 8%–12% of the mean strain rate. It is worthwhile to note here that the significance levels quoted are the probabilities that there are coherent signals at these periods. Given that slow slip may have intrinsic periods of changes in slip rate, it is not guaranteed that this modulation is due to the tides. In Appendix A we look for coherent signals at a wider range of frequencies and find that there are indeed signals at apparently random periods with amplitudes comparable to those at the three weaker tidal periods. However, no other period has a coherent signal as large as that at the M2 period.

[25] Regardless of the nature of the signal at these periods, the data do provide an upper bound on its magnitude, and therefore on the magnitude of tidal modulation. The 90% confidence intervals at all frequencies include only tidal modulation amplitudes less than 40% of the mean strain rate. Assuming that the strain rate is linearly related to the slip rate, there is then a low probability that the tidal modulation causes slip rates on average more than 40% faster than the mean.

4.3. Effects of Modifications to the Fit

[26] The basic idea of our method is to fit a set of sinusoids to the strain data. However, we have introduced several modifications to reduce the error bars as much as possible. Here we summarize the effects of these modifications on the modulation estimates and uncertainties.

4.3.1. Effects of Fit Details and Data Processing

[27] A major assumption in performing our fit is that the phase of the maximum slip rate does not vary with location. As will be seen in section 5.1, there is about a quarter-cycle variability along strike in the semidiurnal tides, and a half-cycle variability in the diurnal tides. Assuming a constant phase is thus strictly incorrect, but we find that the data are unable to constrain a more complicated model. Fitting data from each station individually results in error bars that do not constrain the phase well. Adjusting the relative phase lags at each station to match the computed phase of tidal loading on the plate interface nearby does not significantly improve or worsen the fit to the data, and it does not reduce the scatter in the bootstrap estimates.

[28] Probably the most subjective part of the analysis is choosing segments of the record to use. Fortunately, the exact segment endpoints do not notably affect our conclusions. Increasing or decreasing the segment lengths by up to 0.6 days does not have a significant impact on the results. We have also performed an analysis identical to that presented here, but with data from the four extensometers at each station rather than from the two shear stresses, and therefore necessarily with a new set of segments. Neither the tidal modulation estimates nor the error bars are significantly different.

[29] To help reduce the noise at tidal periods introduced from longer periods by fitting only portions of the record, we highpass filter the data before extracting the segments. The widths of the bootstrap error distributions obtained by fitting segments of filtered data (as in section 4.1) are about 50% smaller than those from fitting unfiltered data. This 50% reduction is important for the marginally significant signal at the S2, O1, and K1 periods, but it is minor for the interpretation of signal at the M2 period.

[30] The difference in modulation estimates from using the different fits can be seen in the first two rows of Figure 5. Independent of the results, equation (5), where the amplitude of tidal modulation is scaled to the mean strain rate, clearly has more physical appeal than equation (3), where the amplitude is forced to be constant. Signal at the M2 period is more significant when we use the scaled fit (Figure 5b), but the results of the two fits are mostly similar. This is probably because the slopes in the different segments are relatively constant. One further aspect of the fit is the additional linear trend (k_m in equations (3) and (5)), included to allow for any residual linear trend in each segment after filtering. The coefficient k_m is consistently small relative to the actual linear trend, and omitting it has a negligible effect on the modulation estimates and error distributions.

4.3.2. Effects of Error Weighting

[31] The largest reduction in uncertainty from our modifications comes from downweighting the misfit by the variance in that segment. This reduces the dependence on very noisy segments and reduces the size of the bootstrap distributions by up to a factor of two. However, this weighting does make interpreting the error distributions more difficult.

[32] One example of this can be seen in Figures 5i–5l. The error distributions found from the non-slow-slip segments are smaller by almost a factor of two than those from bootstrapping and those from the phase randomized slow slip segments. Perhaps a 60% increase in the size of the distributions of modulation parameters can be explained by a larger average variance in the strain data during slow slip (see section 3.4 and Figure 4). The remaining 40% difference is more difficult to explain, as both the weighting scheme and the fit itself play a role. In particular, with this weighting and using equation (5), segments with small variance and large slope have the greatest influence on the resulting modulation parameters, so the smallest variance may be more important to the uncertainty in the modulation parameters than the mean or median variance.

[33] One concern with using this weighting is then that just a few segments, those with the smallest variance or

largest slope, may control the result of the fit. However, this is not the case for the slow slip segments. We obtain similar tidal modulation parameters at the M2 period, albeit with larger error distributions, by performing the bootstrap analysis on various subsets of the data, even if we eliminate those segments with the smallest standard deviation or the smallest ratio of standard deviation to mean strain rate. All of the segments appear to influence the result of the fit and reduce the uncertainty in the modulation estimates, even those with large noise. A bootstrap analysis without the 50% of the segments with the largest ratios of standard deviation to slope results in probability distributions about 20% larger than those from an analysis where they are included.

5. Comparison With Tidal Loading and Tremor

5.1. Tidal Loading Model

5.1.1. Calculations

[34] In order to compare the tidal modulation of the slow slip strain with the stress presumed to cause it, we need to compute the tidal stress on the fault plane due to the ocean loading and solid earth tides. For the ocean loading tides, we compute the stress at depth from a localized increase in water height on the surface from the analytical result for a point load on a homogeneous half space [e.g., *Malvern*, 1969, pp. 561–565], using a Poisson's ratio of 0.25. We use the loading software SPOTL [*Agnew*, 1997] to integrate the stress at depth from the spatially variable ocean height. Since the software is normally used to compute strains on the surface of the Earth, it was necessary to modify it slightly to include shear stress on a horizontal surface and vertical compression, which are nonzero at depth. The global CSR 4.0 model of the ocean tidal heights is used for the Pacific Ocean (updated from CSR 3.0 [*Eanes and Bettadpur*, 1996]), while a regional model is used for the Vancouver area [*Crean et al.*, 1988]. Only the ocean load from less than 5° away is considered. We calculate the integrated stress tensor at each point on a 5 by 5 kilometer grid of the plate interface model of *McCrory et al.* [2004] and then rotate it to obtain the shear and normal components for the local fault plane.

[35] The solid earth body tides are also computed using SPOTL, but here we compute only the stresses at the surface, ignoring any variation with depth. The calculated strains are converted to stresses assuming an isotropic medium with shear modulus of 30 GPa and Poisson's ratio of 0.25. The amplitude and phase of the body tide vary spatially much less than the ocean loading tides, with most of the changes coming from changes in the strike and dip of the subducting slab. The computed body tide stresses are also usually smaller than the ocean loading stresses, with typical amplitudes for the semidiurnal shear stresses of one-tenth to one-half those of the ocean loading stresses. The ocean loading and body tide shear stress amplitudes are more similar in places for the diurnal tides, and the ocean loading fault-normal stresses quickly decay to the magnitude of the body tide away from the water.

[36] Table 2 lists the amplitudes and phases of the shear and normal stresses from the combined ocean loading and body tides at the 5 strongest periods, averaged on the plate interface between 30 and 50 km depth and 46 and 50° north. The amplitudes of the normal stresses are comparable to those of the shear stresses, with a larger normal to shear stress ratio for the diurnal tides. Note that since the listed stresses result from averaging local stresses that are not all in phase, the amplitude at a given location can be a few times larger. This can be seen in Figure 6, where we plot the amplitudes and phases of the calculated stresses on the plate interface for the M2 (12.4 h period) and O1 (25.8 h period) tides, with the indicated phase relative to that of the average tidal shear stress between 30 and 50 km depth. The "Coulomb" stress in the third column of Figure 6 assumes a coefficient of friction of 0.6, and is calculated as the top-to-the-southwest shear stress plus 0.6 times the tensile normal stress, since tensile normal stress is expected to encourage slip.

[37] Over most of the region covered by the borehole strainmeters, the amplitude of the shear stress produced by the M2 tide is several times larger than that of the O1 tide. The phase of the M2 stress varies by about one-quarter cycle along the subduction zone, while the phase of the O1 tide varies by about one-half cycle. The patterns of the phase and amplitude of the M2 and O1 tides are typical of the patterns for the semidiurnal and diurnal tides in this region. The more complicated pattern for the diurnal tides stems from the fact that high tide occurs at the same time in the Strait of Georgia and the Pacific for the diurnal tides but at almost opposite times for the semidiurnal tides. Since simultaneous high water levels in the Pacific and the Strait of Georgia produce normal stresses that are in phase but shear stresses that are out of phase, this results in a higher shear to normal stress ratio for the semidiurnal tides, as also discussed in the work of *Lambert et al.* [2009]. Changes in ocean height in the Juan de Fuca Strait and Puget Sound have an intermediate phase that complicates the tidal loading beneath the Olympic Peninsula.

5.1.2. Comparison With Strain

[38] The phase map for the M2 tide is fortunately relatively simple, and we can compare the phase lags of our observed strain rates with the those of the peak stress on the fault. The peak strain rate for the M2 tidal period plots about halfway between the maximum mean shear stressing rate and the maximum mean shear stress (see Figure 5b). However, the uncertainties associated with the tidal model and the loading calculation, along with the variation of the phase of the tidal stress with location, imply that it could in fact be at either. The peak stress occurs about one-eighth cycle earlier beneath the Olympic Peninsula in our calculations, so the peak strain rate could coincide with peak shear stress if a significant part of the tidal signal comes from that region. And if a significant part of the tidal signal comes from farther inland, or even from beneath southernmost Vancouver Island, where the peak stress occurs later, the maximum strain rate may occur at the peak stressing rate.

[39] On the other hand, the M2 tidal modulation does not appear compatible with peak strain rate occurring at the time of maximum mean tensile normal stress, marked by the dashed lines in Figure 5. As can be seen in Figure 6e, the normal stress in most of the slow slip region is almost exactly out of phase with the maximum strain rate and with the maximum shear stress. There is a region beneath the Juan de Fuca Strait between the 20 and 35 km contours

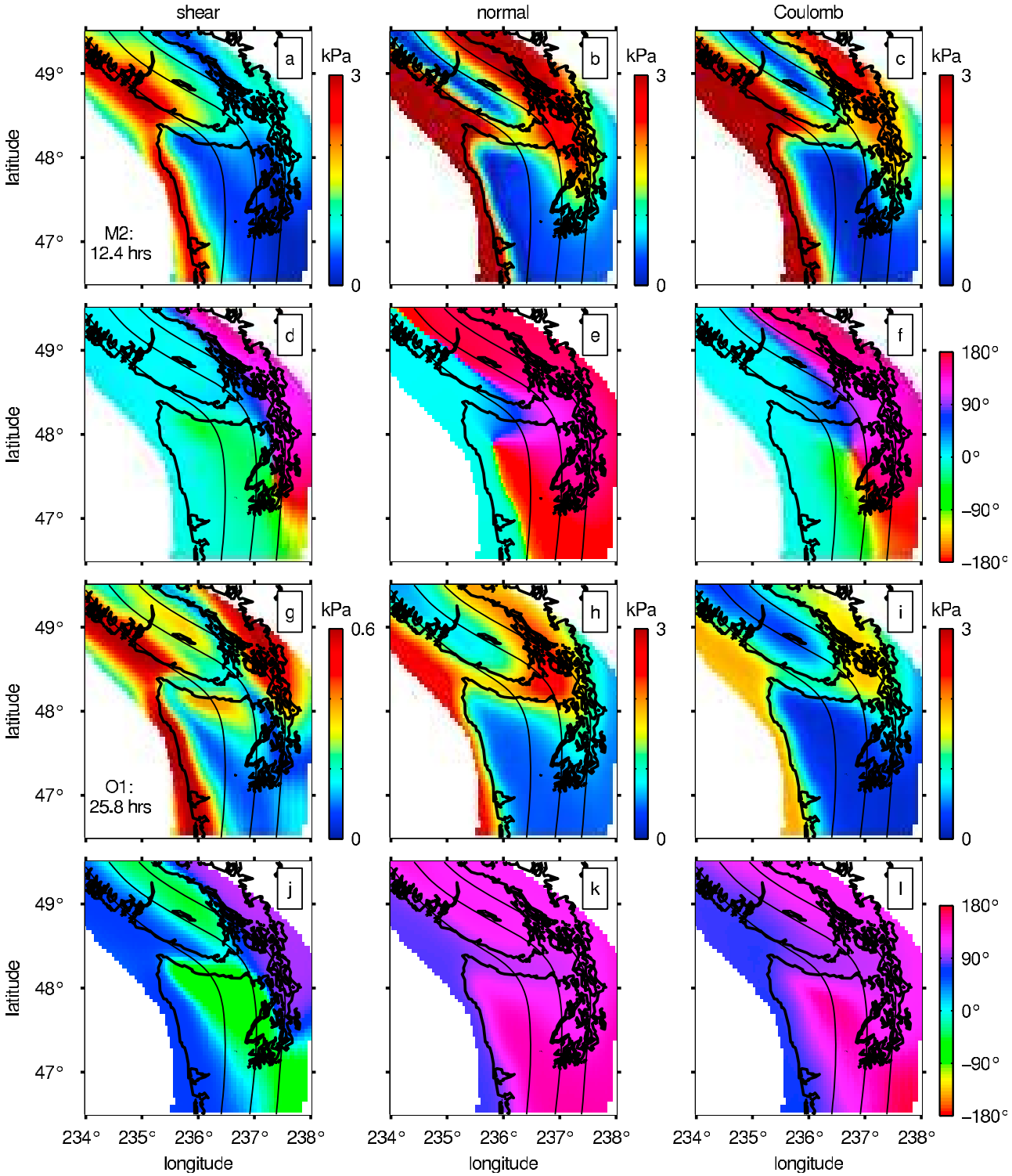

Figure 6. Amplitudes (Figures 6a–6c and Figures 6g–6i) and phase lags (Figures 6d–6f and Figures 6j–6l) of the stresses on the plate interface from the (a–f) M2 and (g–l) O1 ocean loading and solid earth tides. (left) The top-to-the-southwest shear stress, (middle) the tensile normal stress, and (right) the slip-encouraging Coulomb stress. All phase lags are relative to the phase lag of the mean tidal shear stress between −50 and −30 km depth and 46°N and 50°N, as listed in Table 2. Note that the amplitude scale in Figure 6g is different from the other scales. All amplitudes are one-half peak to trough. The black lines are contours of the Juan de Fuca slab interface from *McCrory et al.* [2004] at 30, 40, and 50 km depth.

where the maximum tensile normal stress lags the mean shear stress by about 45°, and the phase of the normal stress is similar to that of shear stress along the western coast of Vancouver Island. So it is possible that the strain rate modulation we observe comes from a response to normal stress, but the observed phase would match the tidal model only if most of the slip occurred beneath the western Juan de Fuca Strait or the western third of Vancouver Island. Given the outlines of slip extent plotted in Figure 1, slip in these locations dominating the signal seems possible but unlikely. In any case, a response to shear stress and not normal stress may not be surprising at this period, as the tidal shear stress is comparable in magnitude and more spatially coherent than the tidal normal stress. It is possible to interpret the phase of the peak strain rate as resulting from the tidal Coulomb stress, plotted in Figures 6c and 6f, assuming a coefficient of friction of 0.6. Depending on the location of slip, the phase of the maximum strain rate at this period may be similar to the timing of tremor in southwest Japan, which appears to occur dominantly between the maximum Coulomb stressing rate and maximum Coulomb stress [*Nakata et al.*, 2008], or to the timing of tremor on the San Andreas, where the maximum tremor rate appears closer to peak shear stress than peak shear stressing rate [*Thomas et al.*, 2009].

[40] While the modulations observed at the S2, K1, and O1 tidal periods are only marginally significant, we nevertheless note that the phase of the S2 tidal loading is very similar in shear and normal stress to that of the M2 loading, so similar considerations apply for its interpretation. The spatial variability of the phase of the shear stress for the O1 and K1 tide make an interpretation more difficult, but if the phase of the observed strain rate is correct, for the maximum strain rate to occur at the maximum shear stress or up to 90° before, most of the signal would have to come from beneath the Olympic Peninsula or below 40 km depth beneath Vancouver Island, the green regions in Figure 6j. A comparison with Figure 1 shows that this is indeed possible though not absolutely necessary. At these periods there is more uncertainty in the observed phase of the maximum strain rate, but the maximum tensile normal stress is again out of phase with the observed maximum strain rate by about 180°, and there is much less spatial variability in the phase of the normal stress for the diurnal tides (see Figure 6k). For these tides the lack of response to normal stress is more surprising, as the normal stress is larger than the shear stress, and the phase of the predicted Coulomb stress is almost entirely controlled by the normal stress.

5.1.3. Lack of Response to Normal Stress?

[41] A similar sensitivity to shear stress and not normal stress has been observed in tidally modulated tremor on the San Andreas Fault [*Thomas et al.*, 2009]. One possible explanation for a lack of response to the normal stress is that changes in normal stress lead to changes in pore pressure if the hydraulic diffusivity is sufficiently low that fluid does not have time to flow on a tidal time scale. We can obtain an upper bound on the magnitude of the pore pressure change by considering the fault zone to contain a set of water-filled cracks aligned parallel to the fault. This is consistent with a model of a planar fault where the true contact area is only a few percent of the fault surface. We may write the fractional change in volume of a crack or array of cracks in response to an applied normal stress $\Delta\sigma$ (tension positive) as

$$\frac{\Delta V}{V} = \kappa \frac{1}{h} L \frac{(\Delta\sigma + \Delta P)}{G/(1-\nu)}, \tag{6}$$

where V is the volume of the crack with length L and thickness h, ΔP is the change in pore pressure, G is the shear modulus, ν is Poisson's ratio, and κ is a constant for the geometry of the crack or cracks. The change in pore pressure in an undrained crack due to this change in volume is given by $\Delta P = -(\Delta V/V)/\beta$, where β is the compressibility of water. Combining this with 6, the change in pressure as a function of the applied normal stress is

$$\Delta P = -\Delta\sigma \left(1 + \frac{\beta G}{\kappa(1-\nu)} \frac{h}{L}\right)^{-1} \tag{7}$$

For an isolated 2-D elliptical crack, the geometric factor κ is 1 [e.g., *Lawn*, 1993]. Assuming a length to thickness ratio L/h of 100, a shear modulus G of 30 GPa, a Poisson's ratio ν of 0.25, and a compressibility of water β at 1 GPa of 2×10^{-10} Pa^{-1}, the magnitude of pore pressure change is slightly more than 90% of the change in normal stress. The change in the effective normal stress, that relevant for friction, is then only one tenth that of the applied stress.

[42] In an array of interacting cracks, the pore pressure changes even more for the same applied stress. For an infinitely repeating array of 2-D cracks with a separation between their centers of W, κ is $2W/(\pi L)\cosh^{-1}(\sec(\pi L/2W))$ [e.g., *Tada et al.*, 2000]. Using the parameters given above, but now assuming an array of cracks where only 10% of the surface is actual contact area (L/W = 0.9), the additional change in pore pressure is about five percent, leading to a change in effective normal stress of less than five percent of the applied stress. For this to be the appropriate explanation for the apparent lack of response to normal stress changes, the pore pressure change would have to be relatively unaffected by diffusion at tidal frequencies.

5.2. Comparison With Tremor

[43] The tremor catalog of *Wech and Creager* [2008] was created with stations mostly located on the Olympic Peninsula and thus has good coverage over much of the slow slip region indicated in Figure 1. *Wech and Creager* [2008] provide the times of overlapping 5 min intervals where they have identified tremor from January 2007 to the present. In Figure 7 we bin these times by phase in the M2 tidal period. There is a clear modulation at this period, and the phase of the maximum tremor rate is within a few degrees of the best fitting maximum strain rate. Both of the observed phases represent some average over the region and over the multiple slow slip events, and their coincidence provides a consistency check on the strain results that is independent of any tidal loading model. The amplitude of tremor rate modulation is also similar to the strain rate modulation, though the comparison is only qualitative, as the tremor rate modulation depends on the detection threshold for tremor. *Rubinstein et al.* [2008] also found a similar amplitude of tidal modulation by stacking the amplitude of the tremor envelope by phase. Making similar histograms

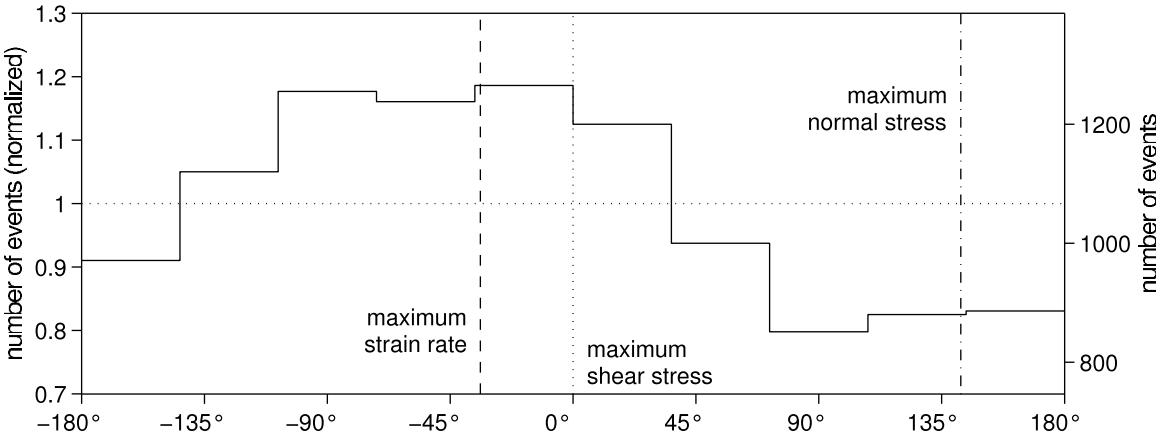

Figure 7. Histogram of the phase lag of tremor events identified by *Wech and Creager* [2008] during the time periods we have identified strain due to slow slip (approximately 24 January to 1 February 2007, 2–9 October 2007, 2–7 March 2008, 2 May to 2 June 2008, 28 April to 3 June 2009). Phase is computed for the 12.4206 h period of the M2 tide and shifted so that 0 is the phase lag of the maximum mean shear stress from Table 2. On the left axis, the number of events per bin is normalized by the mean. The dash-dotted line marks the phase of the maximum fault-normal tensile stress, and the dashed line marks the phase of the maximum strain rate from the previous section.

for the O1 and S2 tidal periods does not reveal significant modulation, though up to about five percent modulation could be concealed by variability in the number of events per bin. Any modulation of tremor by the K1 tide, with a period of about 23.9 h, is obscured by a strong daily signal, presumably from a diurnal variation in the detection threshold for tremor.

6. Summary and Conclusions

[44] We have designed and applied a fit to strain data from Cascadia to identify any tidal modulation of slow slip. The basic premise is to fit a set of sinusoids at the tidal frequencies, but we have introduced a few modifications, the benefits of which are discussed in section 4.3. Regardless of whether or not we use these modifications to the simple sinusoidal fit, the data imply that there is tidal modulation of slow slip-induced strain at the 12.4 h M2 period with close to 90% probability, and the best fitting phase remains in the same quadrant in Figure 5b with or without the preferred weighting and filtering schemes. With the preferred weightings, all of which can be justified on independent grounds, signal at this period is significant at the 99% level. The best fitting amplitude predicts that the slip rate varies on average about 25% above and below the mean during a tidal cycle. The timing of maximum strain rate lies between the calculated maximum shear stressing rate and maximum shear stress, as averaged along strike, but it could be at either or anywhere in between given the quarter-cycle spatial variability in the loading phase. Comparison with a tremor catalog for the region reveals a similarly timed peak in tremor rate at this period.

[45] Modulation estimates at three other tidal periods are smaller, and significant with 70 to 90% probability (and only with the preferred weighting and filtering schemes). These amplitudes are reasonable since the lunar semidiurnal tide is indeed largest in shear stress in this region. However, as seen in Appendix A, there are also signals at several nontidal periods that have amplitudes similar to or larger than those at the S2, O1, and K1 periods. These nontidal signals could be from noise or from real complications in slow slip. None are as large as the modulation at the M2 period.

[46] All of our modulation estimates are rather small. Even at the M2 period, 90% probability distributions constrain the amplitude of modulation to be less than 40% of the mean strain rate. So while these results show that tidal stresses with magnitudes of just a few kPa are able to influence the slip rate in a slow slip event, significant slip appears to occur during all parts of the tidal cycle. These observations should be useful for constraining numerical models of slow slip.

Appendix A: Testing More Frequencies

[47] In previous sections we have considered the frequencies of four of the five tides with largest expected amplitudes and asked whether there is significant signal at these frequencies. Here, we test a wide variety of frequencies to see if those tidal frequencies stand out. We perform 2500 fits to the slow slip data identical to those done earlier, except that each fit uses a single sinusoid with a different frequency. The frequencies used are equally spaced between 0.25 and 5 cycles per day, with a spacing of 0.0019 d^{-1}, and in Figure A1 we plot the amplitude obtained as a function of frequency, after smoothing with a triangular window with half-width 0.03 d^{-1}. This smoothing was chosen because we have found empirically that there is a negative correlation in the amplitudes of a signal at the 12.7 h N2 period and the 12.4 h M2 period, which have a frequency separation of 0.03 d^{-1}, but not between the 12.4 and 12 h periods, which have a frequency separation of 0.06 d^{-1}, nor between any other two tidal frequencies used. The peak near 12.5 h, which we interpret to be associated with the 12.4 h M2 period, is clearly the largest, consistent with our expectations. To better understand the amplitudes from the slow slip segments, we also compute several other curves for comparison.

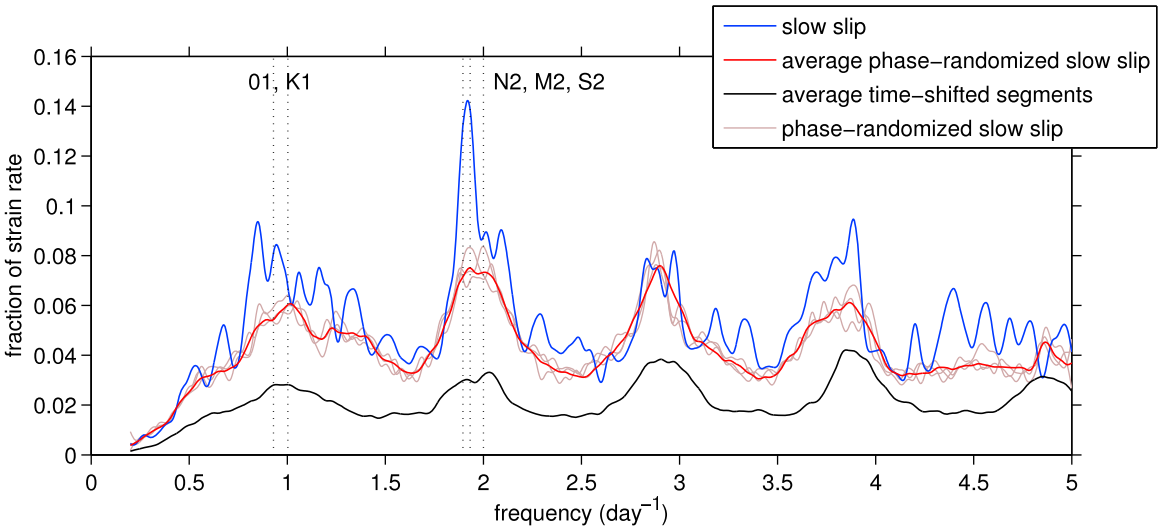

Figure A1. Amplitude of coherent strain rate modulation as a function of frequency. Estimates from the slow slip data are in blue. The pink curves are for three sets of phase randomized slow slip segments, the red curve is the average of 22 such sets, and the black curve is the average of 22 sets of time-shifted segments. The amplitude and phase are computed with a spacing of 0.0019 cycles per day and then smoothed with a triangular window of half-width 0.03 d^{-1} to obtain the curves above. From left to right, the vertical dotted lines are at periods of about 25.8, 23.9, 12.7, 12.4, and 12 h.

[48] First, we compute the amplitudes at a variety of frequencies obtained from portions of the data where we do not expect tidal modulation. As described earlier, the times of all the segments are shifted by a specified amount, and a new set of segments are taken from the data at these times. The new data are fit to obtain an amplitude and phase lag at each frequency as for the slow slip segments. The black curve in Figure A1 is the mean of 22 smoothed curves obtained from sets of segments located 50 to 150 days before and 50 to 150 days after the slow slip segments. As discussed in section 4.1, the smaller amplitudes of these curves are due in part to slightly smaller average variance in non-slow-slip segments, but also in some complex way to a different distribution of variances among the segments. The peaks at roughly integer fractions of one day presumably reflect larger noise or inadequately corrected direct tidal signals at these periods.

[49] For another comparison, we fit the slow slip data at each frequency, but before each set of fits, the times in each segment are given a random shift between 0 and 1.8×10^4 days (without changing the strain data used). Such a random shift should eliminate any correlation between signal in different segments. Each pink curve shows the smoothed amplitudes from fitting the slow slip segments with randomized phase, and the red curve is the mean of 22 such estimates. The amplitudes at the M2, S2, O1, and K1 tidal periods plotted in Figure A1 are roughly equal to the mean amplitudes of the error distributions presented in section 4.1.

[50] The peak we associate with the 12.4 h period M2 tide is by far the strongest at a height of 0.14, well above the background even though it has been diminished by smoothing. The maximum amplitude in this set of frequencies before smoothing was 0.25, at a period of 12.38 h. Of the other tidal periods, only at the 25.8 h O1 period is a peak visible, and there are several other peaks in the slow slip estimates with similar or larger amplitudes at apparently nontidal frequencies. Such occasional peaks exist even for the slow slip segments with randomized phases. Their increased occurrence in the actual slow slip record may be because slow slip does have power, though not necessarily correlated across all events and stations, at a variety of periods in this range.

[51] **Acknowledgments.** We thank Evelyn Roeloffs for advice on processing the PBO strain data and two anonymous reviewers for comments that helped improve the manuscript. This research was supported by NSF grant EAR-0911378. The borehole strainmeter data are provided by the Plate Boundary Observatory operated by UNAVCO for Earthscope and supported by the National Science Foundation (EAR-0350028 and EAR-0732947).

References

Agnew, D. C. (1997), NLOADF: A program for computing ocean-tide loading, *J. Geophys. Res.*, *102*(B3), 5109–5110, doi:10.1029/96JB03458.

Aguiar, A. C., T. I. Melbourne, and C. W. Scrivner (2009), Moment release rate of Cascadia tremor constrained by GPS, *J. Geophys. Res.*, *114*, B00A05, doi:10.1029/2008JB005909.

Crean, P. B., T. S. Murty, and J. A. Stronach (1988), *Mathematical Modelling of Tides and Estuarine Circulation: The Coastal Seas of Southern British Columbia and Washington State*, *Lecture Notes on Coastal and Estuarine Studies*, vol. 30, 471 pp., Springer, New York.

Eanes, R., and S. Bettadpur (1996), The CSR3.0 global ocean tide model: Diurnal and semidiurnal ocean tides from TOPEX/POSEIDON altimetry, *Tech. Rep. CRS-TM-96-05*, Cent. for Space Res., Univ. of Tex., Austin.

Efron, B., and R. Tibshirani (1993), *An Introduction to the Bootstrap*, 1st ed., CRC Press, Boca Raton, Fla.

Gomberg, J., J. L. Rubinstein, Z. G. Peng, K. C. Creager, J. E. Vidale, and P. Bodin (2008), Widespread triggering of nonvolcanic tremor in California, *Science*, *319*(5860), 173–173, doi:10.1126/science.1149164.

Hiramatsu, Y., T. Watanabe, and K. Obara (2008), Deep low-frequency tremors as a proxy for slip monitoring at plate interface, *Geophys. Res. Lett.*, *35*, L13304, doi:10.1029/2008GL034342.

Kao, H., S. Shan, G. Rogers, and H. Dragert (2007), Migration characteristics of seismic tremors in the northern Cascadia margin, *Geophys. Res. Lett.*, *34*, L03304, doi:10.1029/2006GL028430.

Kao, H., S. Shan, H. Dragert, and G. Rogers (2009), Northern Cascadia episodic tremor and slip: A decade of tremor observations from 1997 to 2007, *J. Geophys. Res.*, *114*, B00A12, doi:10.1029/2008JB006046.

Lambert, A., H. Kao, G. Rogers, and N. Courtier (2009), Correlation of tremor activity with tidal stress in the northern Cascadia subduction zone, *J. Geophys. Res.*, *114*, B00A08, doi:10.1029/2008JB006038.

Lawn, B. (1993), *Fracture of Brittle Solids*, 2nd ed., Cambridge Univ. Press, New York.

Liu, C., A. T. Linde, and I. S. Sacks (2009), Slow earthquakes triggered by typhoons, *Nature*, *459*(7248), 833–836, doi:10.1038/nature08042.

Maeda, T., and K. Obara (2009), Spatiotemporal distribution of seismic energy radiation from low-frequency tremor in western Shikoku, Japan, *J. Geophys. Res.*, *114*, B00A09, doi:10.1029/2008JB006043.

Malvern, L. E. (1969), *Introduction to the Mechanics of a Continuous Medium*, 713 pp., Prentice-Hall, Englewood Cliffs, N. J.

McCausland, W., P. G. Silver, and E. Roeloffs (2008), Which came first, the tremor or the slip, and is there slip-free tremor in Cascadia?, *Eos Trans. AGU*, *90*(48), Fall Meet. Suppl., Abstract U32A–03.

McCrory, P. A., J. L. Blair, D. H. Oppenheimer, and S. R. Walter (2004), Depth to the Juan de Fuca slab beneath the Cascadia subduction margin—A 3-D model for sorting earthquakes, *U.S. Geol. Surv. Tech. Rep.*, *91*,

Miyazawa, M., and E. E. Brodsky (2008), Deep low-frequency tremor that correlates with passing surface waves, *J. Geophys. Res.*, *113*, B01307, doi:10.1029/2006JB004890.

Nakata, R., N. Suda, and H. Tsuruoka (2008), Nonvolcanic tremor resulting from the combined effect of Earth tides and slow slip events, *Nat. Geosci.*, *1*, 676–678, doi:10.1038/ngeo288.

Obara, K., H. Hirose, F. Yamamizu, and K. Kasahara (2004), Episodic slow slip events accompanied by nonvolcanic tremors in southwest Japan subduction zone, *Geophys. Res. Lett.*, *31*, L23602, doi:10.1029/2004GL020848.

Rogers, G., and H. Dragert (2003), Episodic tremor and slip on the Cascadia subduction zone: The chatter of silent slip, *Science*, *300*(5627), 1942–1943, doi:10.1126/science.1084783.

Rubinstein, J. L., J. E. Vidale, J. Gomberg, P. Bodin, K. C. Creager, and S. D. Malone (2007), Nonvolcanic tremor driven by large transient shear stresses, *Nature*, *448*(7153), 579–582, doi:10.1038/nature06017.

Rubinstein, J. L., M. L. Rocca, J. E. Vidale, K. C. Creager, and A. G. Wech (2008), Tidal modulation of nonvolcanic tremor, *Science*, *319*(5860), 186–189, doi:10.1126/science.1150558.

Rubinstein, J. L., J. Gomberg, J. E. Vidale, A. G. Wech, H. Kao, K. C. Creager, and G. Rogers (2009), Seismic wave triggering of nonvolcanic tremor, episodic tremor and slip, and earthquakes on Vancouver Island, *J. Geophys. Res.*, *114*, B00A01, doi:10.1029/2008JB005875.

Schwartz, S. Y., and J. M. Rokosky (2007), Slow slip events and seismic tremor at circum-Pacific subduction zones, *Rev. Geophys.*, *45*, RG3004, doi:10.1029/2006RG000208.

Shelly, D. R., G. C. Beroza, and S. Ide (2007), Complex evolution of transient slip derived from precise tremor locations in western Shikoku, Japan, *Geochem. Geophys. Geosyst.*, *8*, Q10014, doi:10.1029/2007GC001640.

Tada, H., P. C. Paris, and G. R. Irwin (2000), *The Stress Analysis of Cracks Handbook*, 3rd ed., Am. Soc. of Eng., New York.

Thomas, A. M., R. M. Nadeau, and R. Burgmann (2009), Tremor-tide correlations and near-lithostatic pore pressure on the deep San Andreas fault, *Nature*, *462*(7276), 1048–1051, doi:10.1038/nature08654.

Wang, K., H. Dragert, H. Kao, and E. Roeloffs (2008), Characterizing an "uncharacteristic" ETS event in northern Cascadia, *Geophys. Res. Lett.*, *35*, L15303, doi:10.1029/2008GL034415.

Wech, A. G., and K. C. Creager (2008), Automated detection and location of Cascadia tremor, *Geophys. Res. Lett.*, *35*, L20302, doi:10.1029/2008GL035458.

Wech, A. G., K. C. Creager, and T. I. Melbourne (2009), Seismic and geodetic constraints on Cascadia slow slip, *J. Geophys. Res.*, *114*, B10316, doi:10.1029/2008JB006090.

J. C. Hawthorne and A. M. Rubin, Department of Geosciences, Princeton University, Washington Road, Princeton, NJ 08540, USA. (jchawtho@princeton.edu; arubin@princeton.edu)